Moore, J.C., and Klaus, A. (Eds.)
Proceedings of the Ocean Drilling Program, Scientific Results Volume 171A

1. Data Report: Quantitative Image Analysis of Relative Porosity Contributions in the Décollement and Proto-décollement, Northern Barbados Accretionary Prism[1]

Glen S. Wallace[2]

INTRODUCTION

This study quantitatively addresses the significance of porosity within radiolarian tests in the décollement zone at the toe of the northern Barbados accretionary prism. Quantification was accomplished using scanning electron microscope images of core samples taken from Ocean Drilling Program (ODP) Sites 671 and 672, representing the décollement and proto-décollement, respectively. The décollement is localized to a radiolarian claystone, and its depth correlates with a low-density anomaly that has been attributed to high porosity at all relevant ODP drilling sites in the area (Moore, Klaus, et al., 1998; Shipley, Ogawa, Blum, et al., 1995; Mascle, Moore, et al., 1988). Porosity in the décollement zone is presumably lost between Sites 672 and 671 because of shear enhanced consolidation (Moore et al., 1998).

METHODS

Sample Selection and Preparation

Fifty-one oriented samples were taken in the depth interval of the décollement and proto-décollement at Sites 671 and 672. Sample locations were selected with an emphasis on avoiding drilling induced deformation. Samples taken from Site 671 have core-scale fabrics rang-

[1]Wallace, G.S., 2000. Data report: Quantitative image analysis of relative porosity contributions in the décollement and proto-décollement, northern Barbados accretionary prism. *In* Moore, J.C., and Klaus, A. (Eds.), *Proc. ODP, Sci. Results,* 171A, 1–19 [Online]. Available from World Wide Web: <http://www-odp.tamu.edu/publications/171A_SR/VOLUME/CHAPTERS/SR171A01.PDF>. [Cited YYYY-MM-DD]
[2]Department of Earth Sciences, 1156 High Street, University of California, Santa Cruz, Santa Cruz CA 95064, USA. (Present address: Department of Geological Sciences, University of Washington, 63 Johnson Hall, Seattle WA 98195, USA. **gsw@u.washington.edu**)

Initial receipt: 27 April 1999
Acceptance: 30 September 1999
Web publication: 11 August 2000
Ms 171ASR-102

ing from scaly to apparently intact. Samples show a mixture of sheared and intact material down to the micrometer scale, as noted earlier by Labaume et al. (1997).

Two types of samples were prepared for this study. One set was oven dried, broken to an undisturbed surface, and gold coated for scanning electron microscope (SEM) examination for a qualitative three-dimensional perspective of fabrics (Figs. F1, F2). A second, larger set of samples was prepared using a resin impregnation process (Swartz and Lindsley-Griffen, 1990; Jim, 1985), to give an effectively two-dimensional surface for quantitative image analysis and general examination (Figs. F3, F4, F5, F6, F7, F8, F9, F10). Resin-impregnated samples were soaked in acetone for 4 weeks in order to replace pore water in preparation for impregnation with low-viscosity resin. Acetone saturation is preferable to water because resin is miscible in acetone and aids impregnation. Once samples were saturated with acetone, the excess acetone was carefully removed from the sample vessel, and the vessel was filled with Spurr low-viscosity resin. Impregnation was conducted under vacuum to reduce contact between oxygen and the Spurr resin, which increases its viscosity with exposure to oxygen. Samples were soaked in resin for 2 weeks and cured in a vacuum over 5 days using a stepped-temperature schedule, with care not to exceed 60°C to prevent cracking. After samples were allowed to cool, they were cut under kerosene, and polished with 1-µm grit under alcohol and oils.

Image Analysis

Images were captured digitally with a 4096 pixel × 4096 pixel image size, to maximize resolution for analysis. Care was taken to capture at random locations to avoid selective bias. Porosity in radiolarian tests was manually selected on a separate graphical layer and quantified. Voids in images related to radiolarian tests (Fig. F3) were selected, but areas of voids that were infilled by precipitates (Fig. F10) or injected sediment were excluded. Output from this image analysis was the percent of sample area that is radiolarian-related porosity (Tables T1, T2).

A similar technique was used for images used to determine interparticle porosity in the sediment matrix. Images were acquired at higher magnification so that individual clay particles and voids could be adequately quantified (Figs. F4, F5, F7). Void spaces were selected using a combination of thresholding and density slicing (Table T3).

Qualitatively, radiolarian-related porosity measurements have errors of ±10%, whereas interparticle porosity measurements in the bulk matrix have errors of ±15%. Error is higher in the clay measurements because of the smaller number of samples that could be effectively used for analysis and the lower accuracy of the selection method.

RESULTS/CONCLUSIONS

At the level of the proto-décollement at Site 672, radiolarian-related porosity ranges from 0.2% to 8.5%, with a mean of 3.9%. At the level of the décollement in Site 671, radiolarian-related porosity ranges between 0% and 4.6%, with a mean of 1.1%. Interparticle clay porosity in the bulk sediment matrix has a mean of 6.5% in the proto-décollement at Site 672 and decreases to a mean of 3.2% in the décollement at Site 671. Comparison of the observed changes in porosity between Sites 672 and 671 indicates that porosity loss in the bulk sediment matrix is more sig-

F1. Broken-surface sample of the relatively intact nature of the radiolarian tests and the preservation of macropores of the proto-décollement, p. 6.

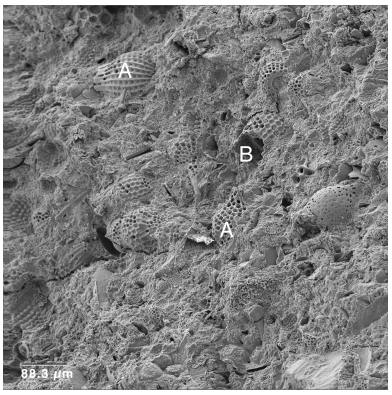

F2. Broken-surface sample of the structurally intact nature of the radiolarian tests of the proto-décollement, p. 7.

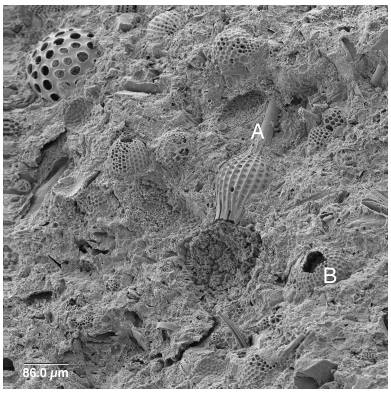

F3. Polished section from the proto-décollement showing the distribution of radiolarian macroporosity, p. 8.

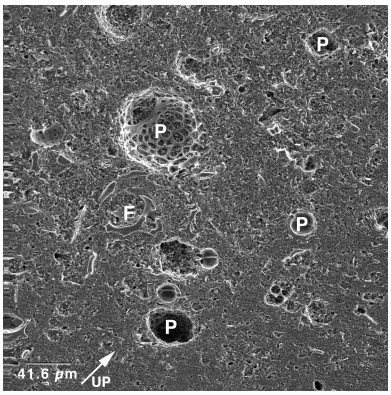

nificant than loss of radiolarian-related porosity. It is possible that some fabrics are undersampled because of the degree of drilling induced deformation, which may preferentially localize in one type of fabric, and the difficulty of assessing microscopic fabrics based on in situ core-scale observations during initial sampling. However, considering both the range of values and the difference in the average values for the decrease in radiolarian-related porosity compared to porosity loss in the sediment matrix, the results would probably not be significantly altered by these biases. A detailed discussion of these data will be presented in another publication.

ACKNOWLEDGMENTS

This research was made possible by funding from the United States Science Support Program and National Science Foundation grant number OCE-9618166. I would like to thank Jonathan Krupp for help with microscope work and Bruce Tanner for help with sample preparation.

F4. Close-up image showing matrix fabric in the proto-décollement, p. 9.

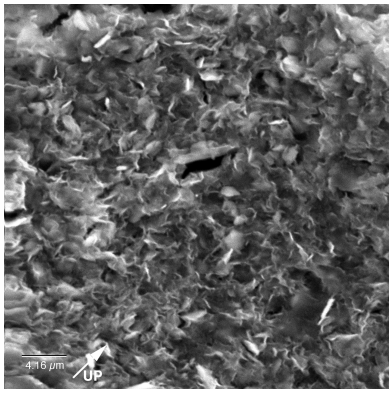

F5. Close-up image of the clay fabric found in proto-décollement, p. 10.

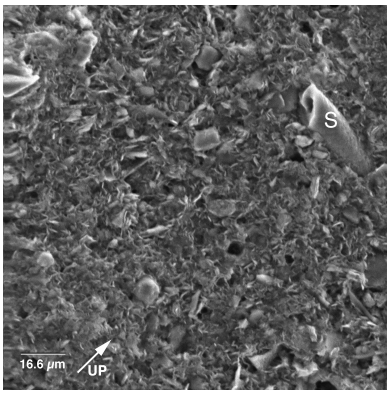

F6. Close-up image showing the character of the clay fabric in and out of a clay-filled radiolarian test, p. 11.

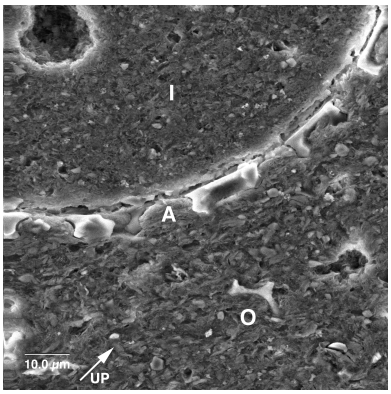

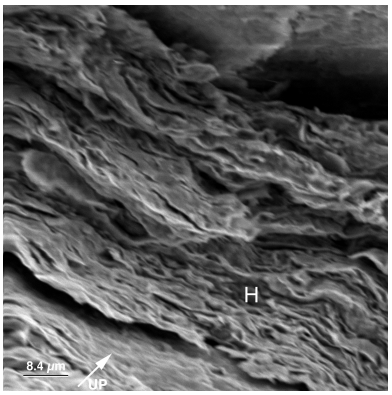

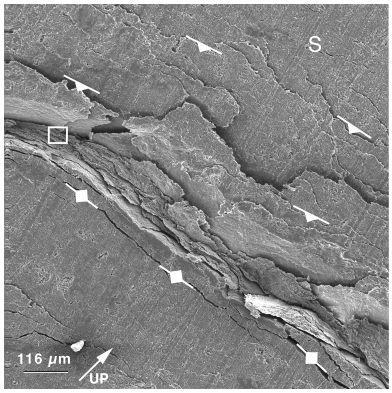

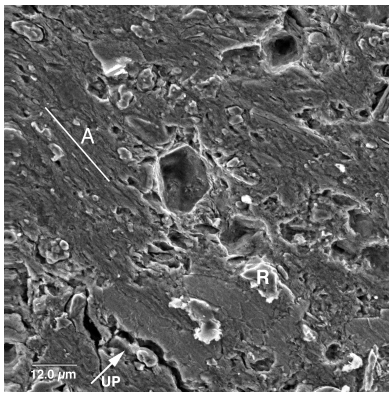

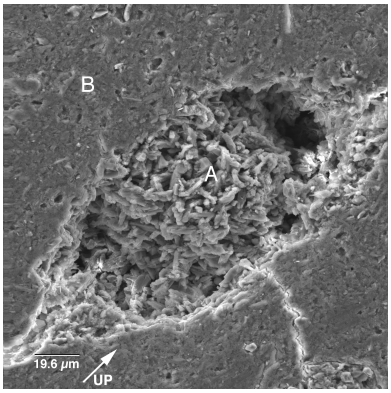

REFERENCES

Jim, C.Y., 1985. Impregnation of moist and dry unconsolidated clay samples using Spurr resin for microstructural studies. *J. Sediment. Petrol.,* 55:597–599.

Labaume, P., Maltman, A.J., Bolton, A., Tessier, D., Ogawa, Y., and Takizawa, S., 1997. Scaly fabrics in sheared clays from the décollement zone of the Barbados accretionary prism. *In* Shipley, T.H., Ogawa, Y., Blum, P., and Bahr, J.M. (Eds.), *Proc. ODP, Sci. Results,* 156: College Station, TX (Ocean Drilling Program), 59–77.

Mascle, A., Moore, J.C., et al., 1988. *Proc. ODP, Init. Repts.,* 110: College Station, TX (Ocean Drilling Program).

Moore, J.C., Klaus, A., Bangs, N.L., Bekins, B., Bucker, C.J., Bruckmann, W., Erickson, S.N., Hansen, O., Horton, T., Ireland, P., Major, C.O., Moore, G.F., Peacock, S., Saito, S., Screaton, E.J., Shimeld, J.W., Stauffer, P.H. Taymaz, T., Teas, P.A., Tokunaga, T., 1998. Consolidation patterns during initiation and evolution of a plate-boundary décollement zone: Northern Barbados accretionary prism. *Geology,* 26:811–814.

Moore, J.C., Klaus, A., et al., 1998. *Proc. ODP, Init. Repts.,* 171A: College Station, TX (Ocean Drilling Program).

Shipley, T.H., Ogawa, Y., Blum, P., et al., 1995. *Proc. ODP, Init. Repts.,* 156: College Station, TX (Ocean Drilling Program).

Swartz, J.F., and Lindsley-Griffin, N., 1990. An improved impregnation technique for studying structure of unlithified cohesive sediments. *In* Suess, E., von Huene, R., et al., *Proc. ODP, Sci. Results,* 112: College Station, TX (Ocean Drilling Program), 87–91.

Figure F1. Broken-surface sample showing the gross fabric of the proto-décollement (Section 110-672A-22X-3). Note (**A**) the relatively intact nature of the radiolarian tests and (**B**) the preservation of macropores. Orientation is not preserved. Scale bar = 88.3 µm.

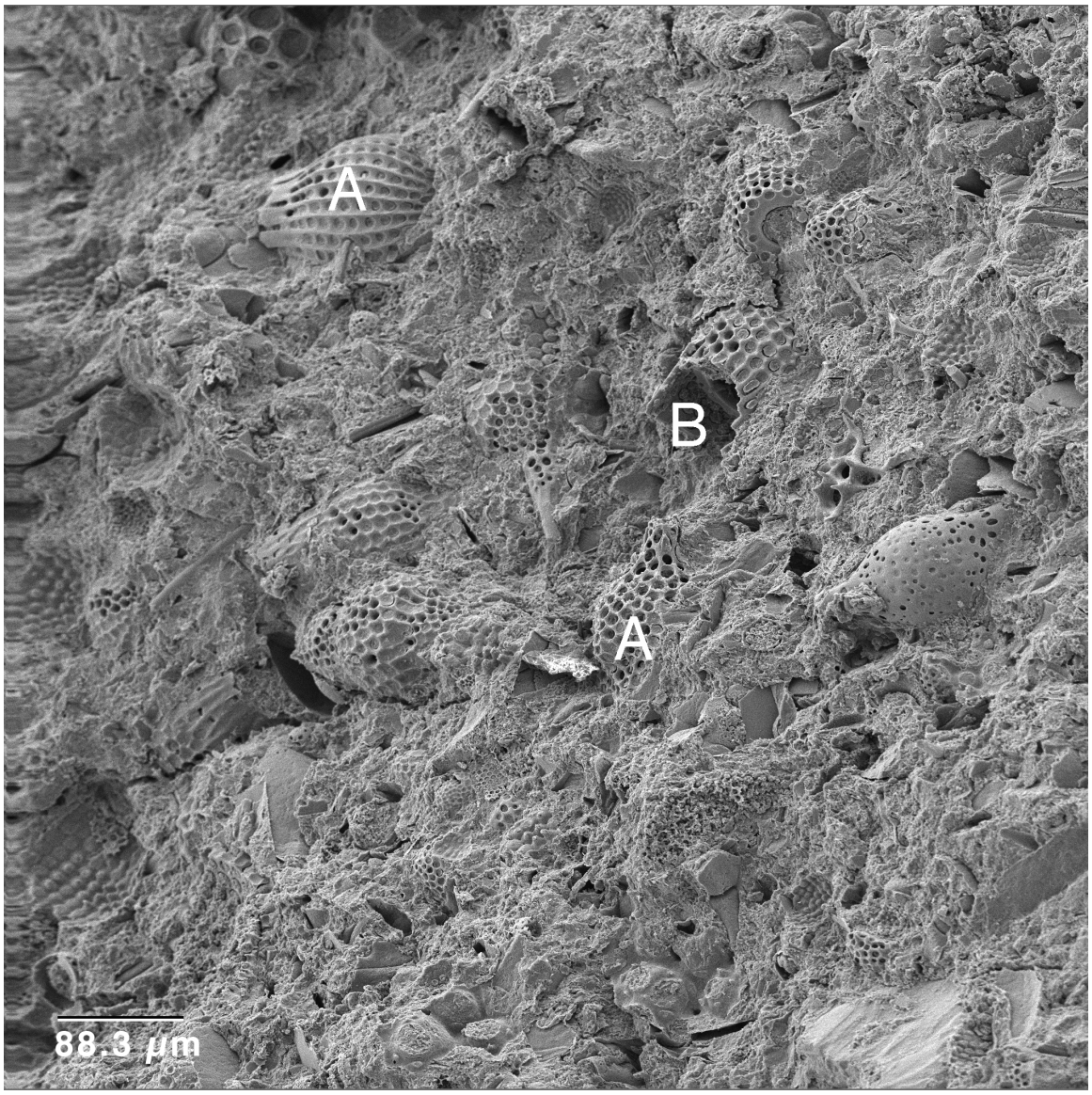

Figure F2. Broken-surface sample showing the gross fabric of the proto-décollement (Section 110-672A-22X-3). Note the structurally intact nature of the radiolarian tests, most notably (**A**) the intact apical spine and (**B**) the preservation of radiolarian macropores. Orientation is not preserved. Scale bar = 86.0 µm.

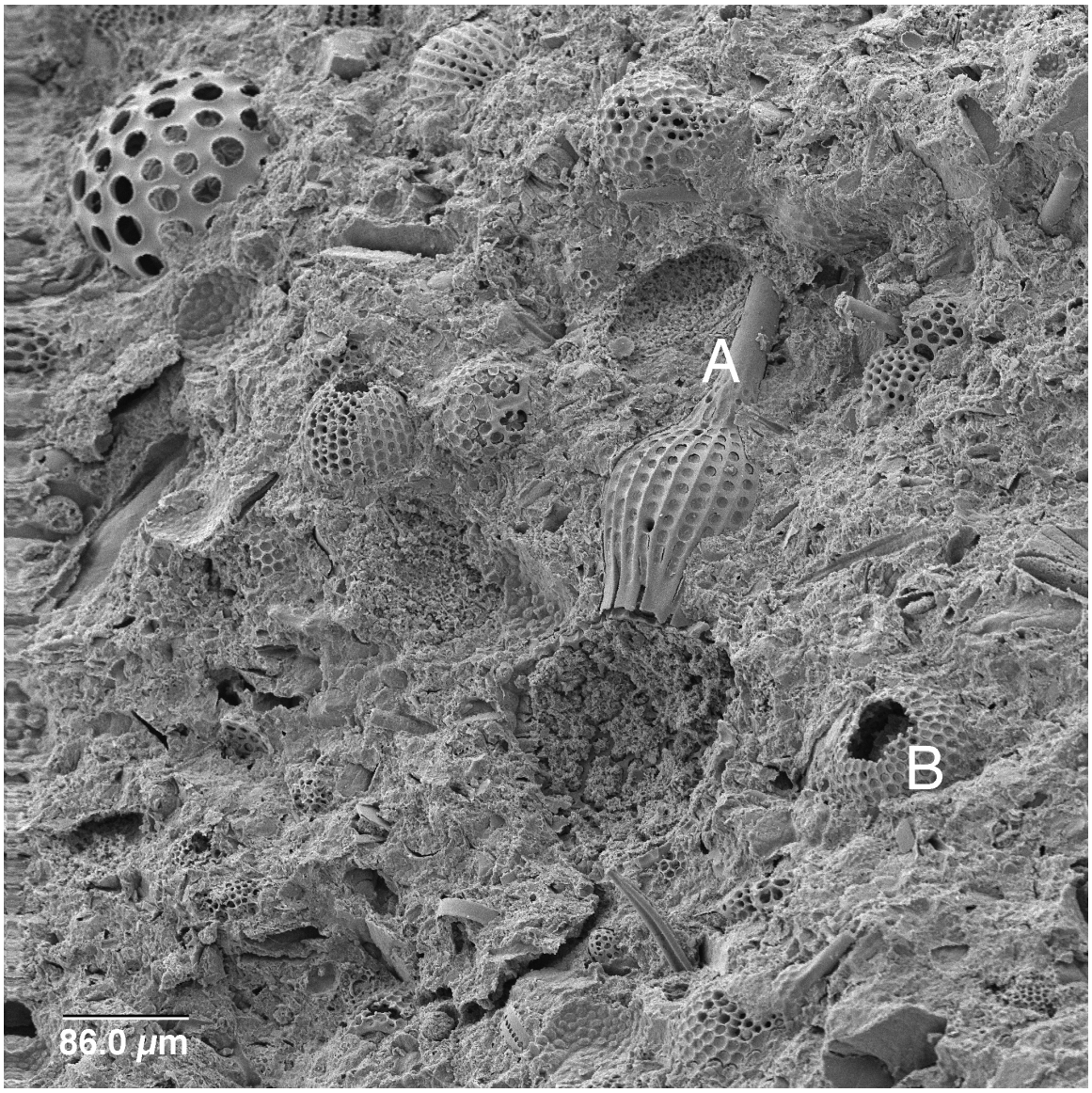

Figure F3. Polished section from the proto-décollement showing the distribution of radiolarian macroporosity (Section 110-672A-22X-2). P = radiolarian-related porosity; F = radiolarian test fragment. Radiolarian tests are supported in the clay matrix and have test-to-test contact only in isolated localities. It should be noted that this image exhibits a large amount of radiolarian-related porosity compared to most of the images used for quantitative analysis. Orientation is shown next to the scale bar. Scale bar = 41.6 µm.

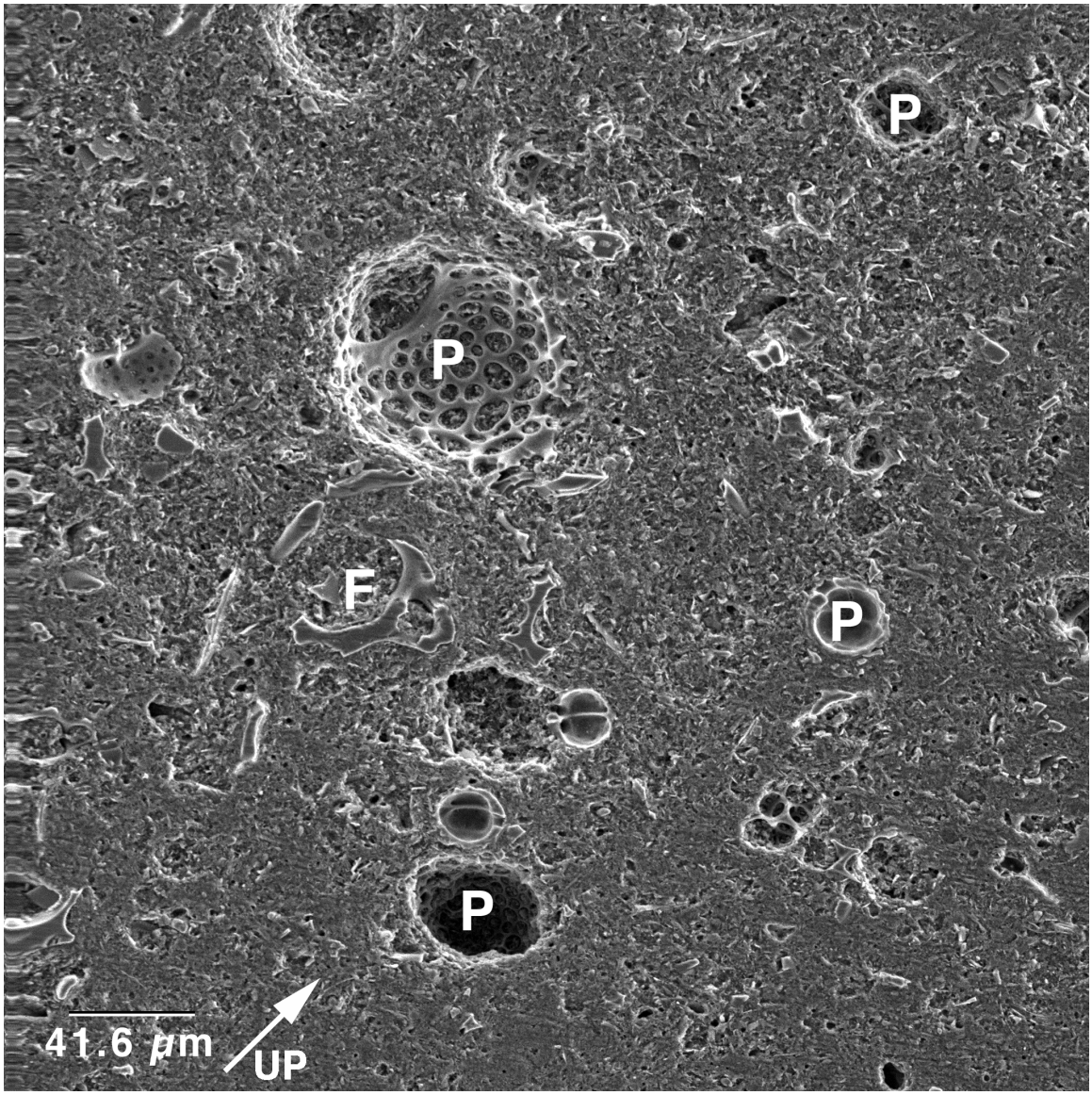

Figure F4. Close-up image showing matrix fabric in the proto-décollement, characterized by flocculated clay particles with high interparticle porosity (Section 110-672A-20X-2). Orientation is diagonally up and to the right. Scale bar = 4.16 µm.

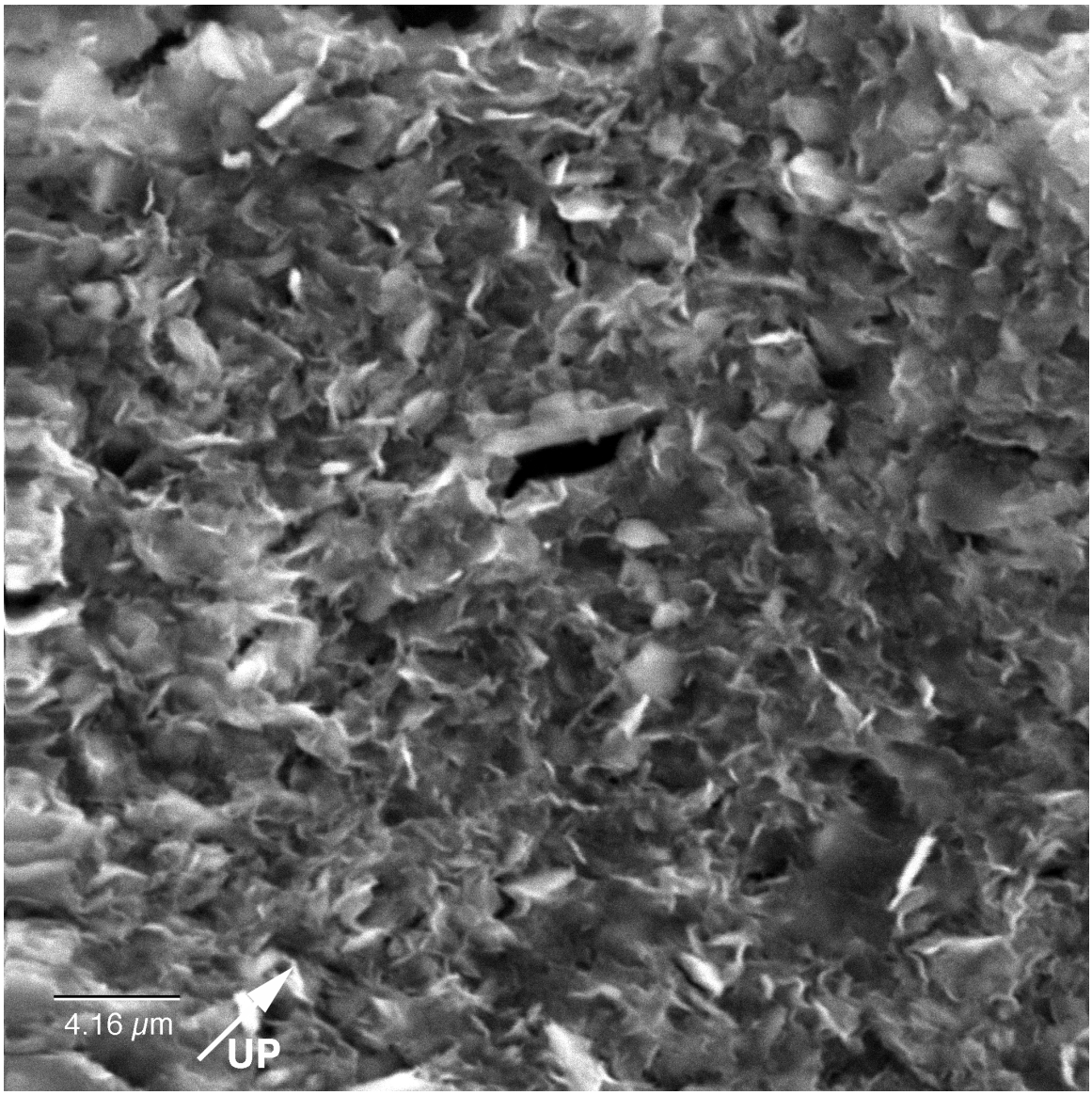

Figure F5. Close-up image of the clay fabric found in the proto-décollement, characterized by edge-to-edge and edge-to-face contacts and associated high interparticle porosity (Section 110-672A-22X-2). The cylindrical object (S) in the left side of the frame is most likely a sponge spicule. Orientation is shown next to the scale bar. Scale bar = 16.6 µm.

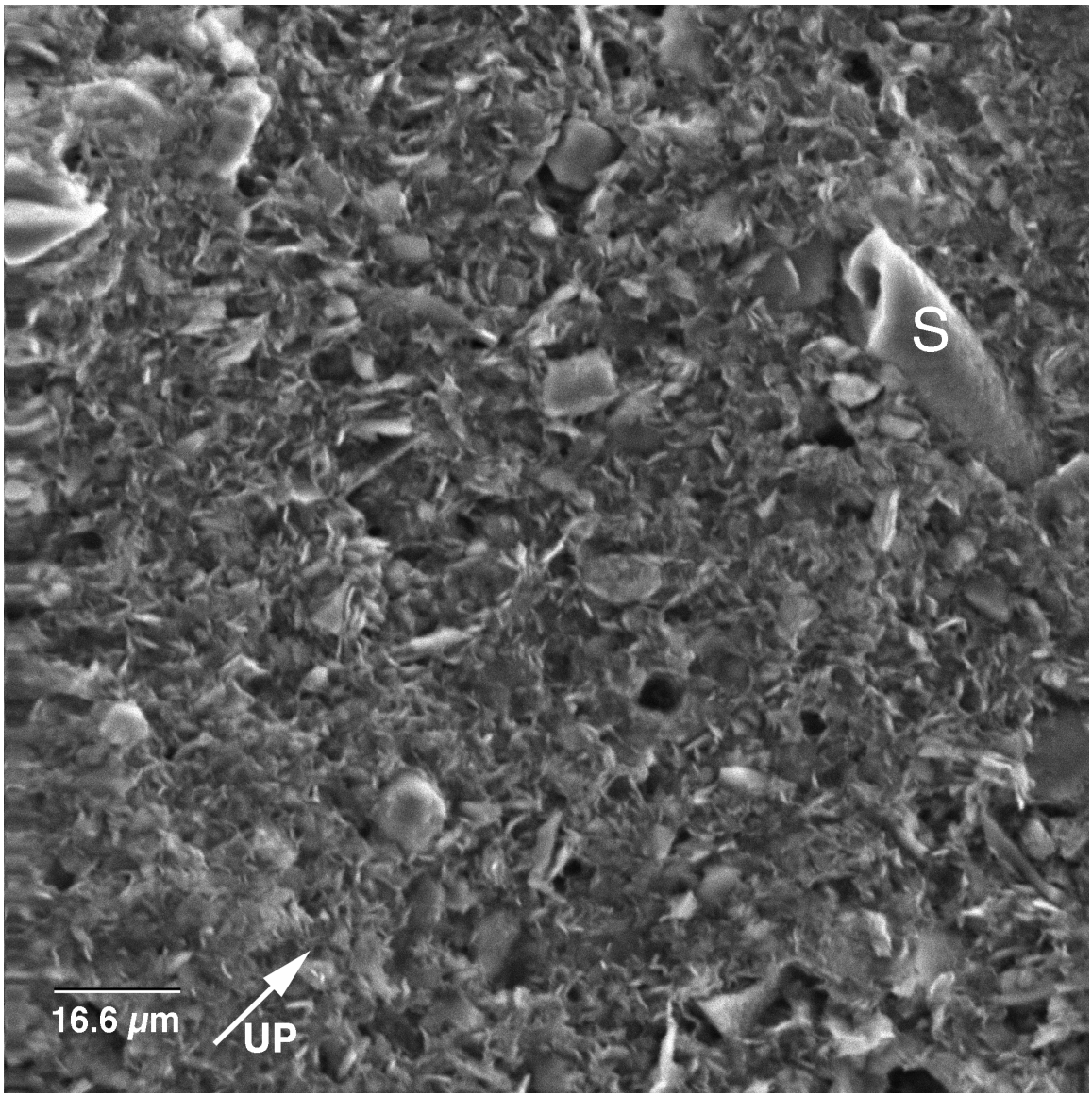

Figure F6. Close-up image showing the character of the clay fabric in (I) and out (O) of a clay-filled radiolarian test (Section 110-672A-22X-3). Particles are flocculated inside and outside of the test, with the exception of the outside borders of the test in which local stress concentrations have oriented grains (A). Also, grain size inside the test appears to be generally smaller than outside. Orientation is shown next to the scale bar. Scale bar = 10.0 µm.

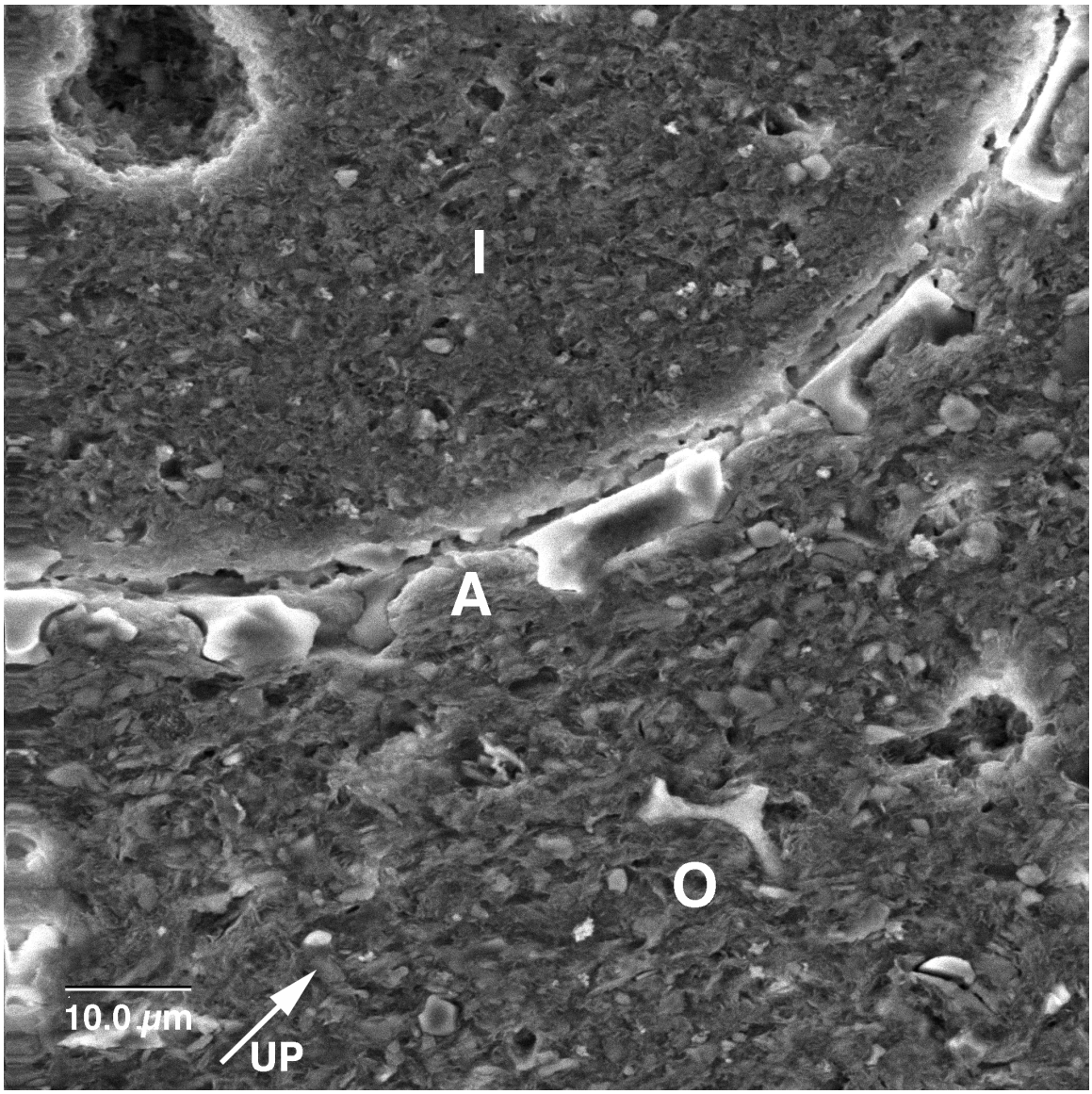

Figure F7. Subhorizontal fabric (clearest at H) associated with shearing in the décollement, characterized by lower porosity and face-to-face and edge-to-face grain contacts (Section 110-671B-55X-6). Orientation is shown next to the scale bar. Scale bar = 8.4 µm.

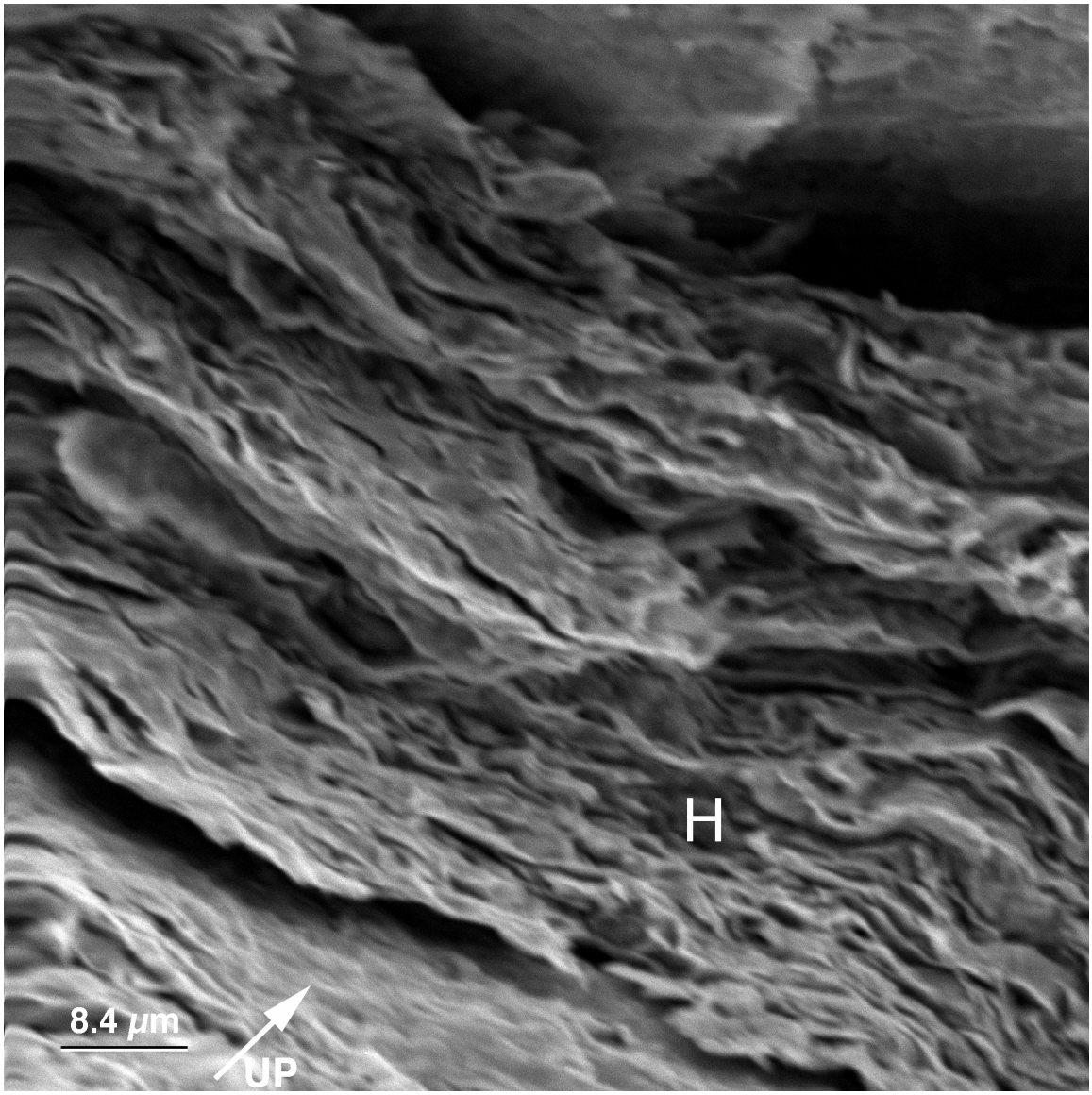

Figure F8. Larger-scale view of Figure F7, p. 12, demonstrating the penetrative relationship between micrometer-scale clay orientations and observed macroscopic scaly fabrics in the décollement (Section 110-671B-55X-6). The inset box marks the location of Figure F7, p. 12. Note the total lack of radiolarian-related porosity. Foliations are marked relative to the plane of the image. The appearance of two planes of foliation is a result of looking along the approximate slip direction in an S-C type fabric (S = foliation, C = shear or cisaillement surface). Striations on planar surface (S) are an artifact of sample preparation. Scale bar = 116 µm.

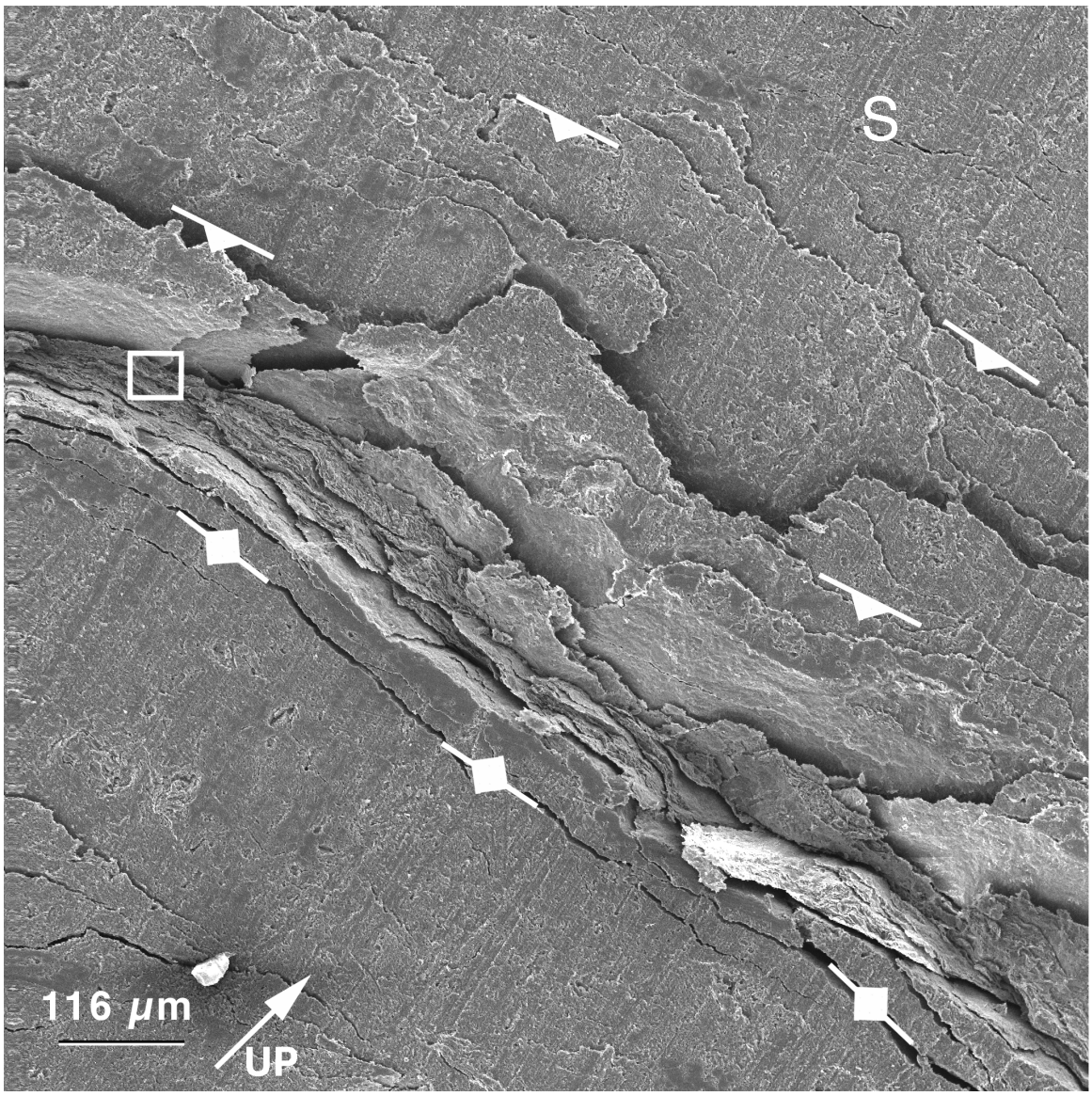

Figure F9. Close-up image showing subhorizontal orientations of clay particles and entrained fragments of radiolarian tests (R) (Section 110-671B-56X-5). Test fragments are identified on the basis of morphology and qualitative X-ray measurements taken during SEM observations using an energy dispersive system. The line next to A is drawn parallel to the subhorizontal bulk sediment fabric. Orientation is shown next to the scale bar. Scale bar = 12.0 µm.

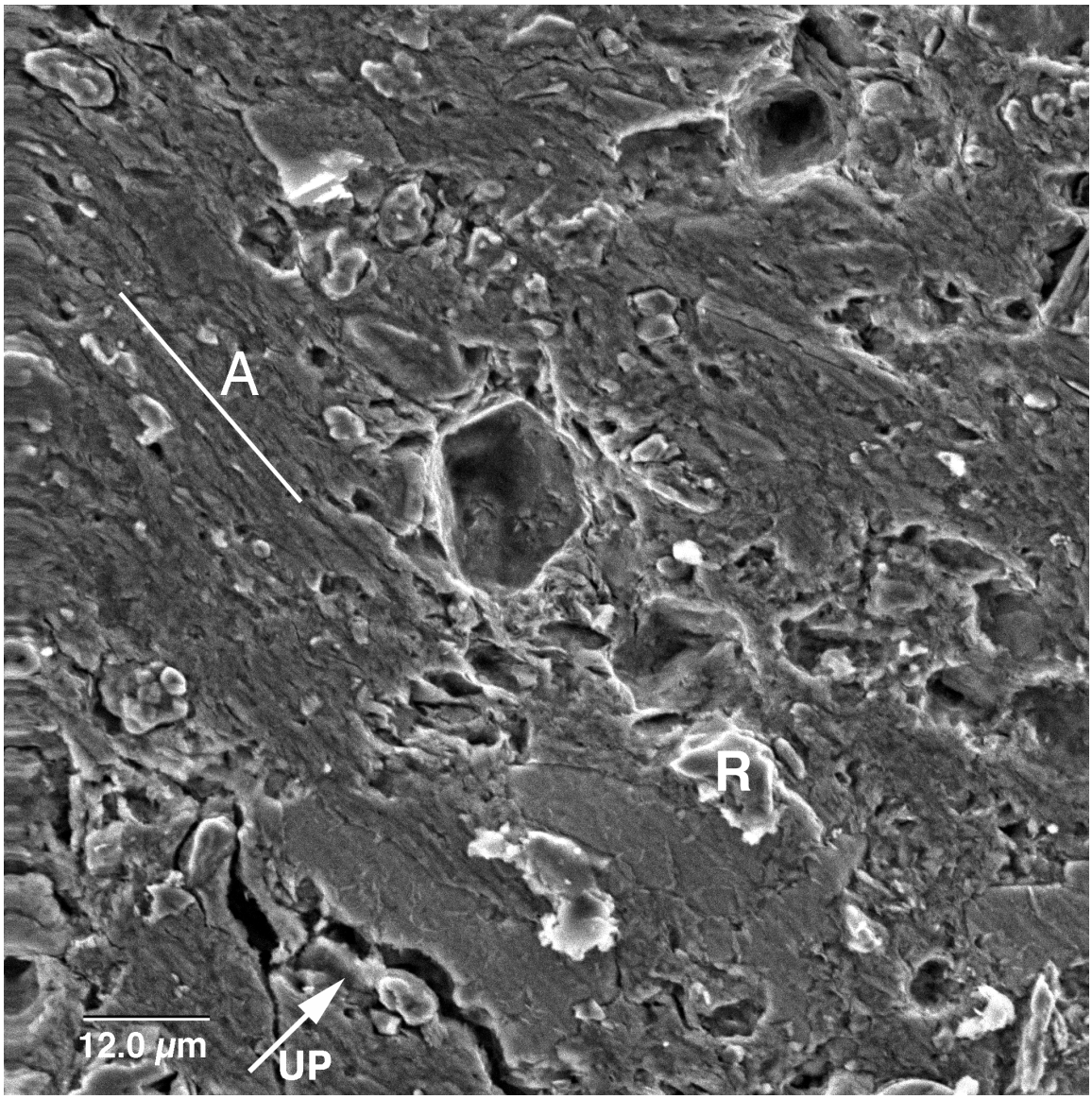

Figure F10. Dissolved and zeolite-infilled radiolarian test in a low-strain portion of the décollement (Section 110-671C-2X-CC). A = radiolarian-related pore infilled with an authigenic zeolite crystal lattice. B = the bulk sediment matrix. Orientation is shown next to the scale bar. Scale bar = 19.6 µm.

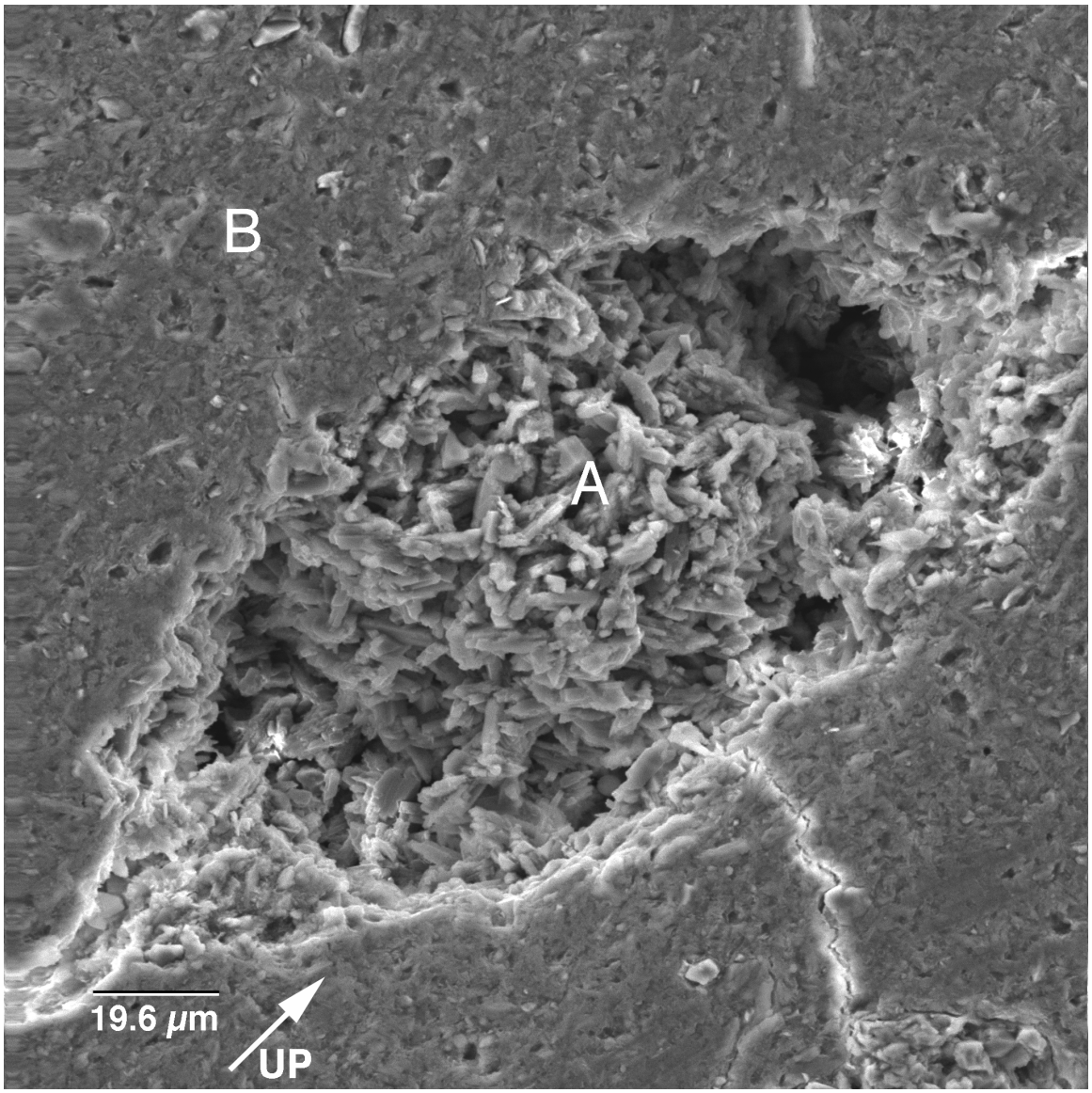

Table T1. Radiolarian-related porosity data for the proto-décollement, Site 672. (Continued on next page.)

Core, section, interval (cm)	Depth (mbsf)	Not radiolarian-related porosity pixels	Radiolarian-related porosity pixels	Area radiolarian-related porosity (%)	Average area radiolarian-related porosity (%)	Average radiolarian-related porosity descriptive statistics	
110-672A-							
19X-1, 41-43	161.7	4,179,530	14,774	0.35	0.39	Count	27
19X-1, 41-43	161.7	4,176,949	17,355	0.41		Maximum	8.48%
19X-1, 41-43	161.7	4,177,907	16,397	0.39		Mean	3.90%
19X-2, 27-30	163.1	4,032,135	162,169	3.87	3.37	Median	3.56%
19X-2, 27-30	163.1	4,016,930	177,374	4.23		Minimum	0.19%
19X-2, 27-30	163.1	4,110,223	84,081	2.00		Range	8.29%
19X-3, 42-45	164.7	4,171,009	23,295	0.56	0.82	Standard deviation	2.70%
19X-3, 42-45	164.7	4,153,361	40,943	0.98			
19X-3, 42-45	164.7	4,155,631	38,673	0.92			
19X-5, 128-130	168.6	4,150,509	43,795	1.05	1.05		
19X-5, 128-130	168.6	4,151,519	42,785	1.04			
19X-5, 128-130	168.6	4,150,069	44,235	1.08			
19X-CC, 2-4	169.0	3,869,126	325,178	7.81	4.03		
19X-CC, 2-4	169.0	4,094,815	99,489	2.37			
19X-CC, 2-4	169.0	4,113,882	80,422	1.92			
20X-2, 48-50	172.8	1,037,287	11,289	1.08	0.62		
20X-2, 48-50	172.8	4,187,186	7,118	0.17			
20X-1, 117-120	172.0	4,137,211	57,093	1.36	0.52		
20X-1, 117-120	172.0	4,190,228	4,076	0.10			
20X-1, 117-120	172.0	4,190,753	3,551	0.09			
20X-3, 28-130	175.1	4,108,956	85,348	2.03	1.48		
20X-3, 128-130	175.1	4,153,616	40,688	1.01			
20X-3, 128-130	175.1	4,136,478	57,826	1.40			
20X-CC, 27-30	175.6	3,993,405	200,899	4.85	3.36		
20X-CC, 27-30	175.6	4,045,037	149,267	3.56			
20X-CC, 27-30	175.6	4,123,798	70,506	1.68			
21X-2, 122-127	183.0	4,194,304	0	0.00	6.85		
21X-2, 122-127	183.0	3,619,651	574,653	13.70			
21X-1, 121-124	181.5	3,851,966	342,338	8.16	7.61		
21X-1, 121-124	181.5	3,897,857	296,447	7.07			
21X-3, 120-123	184.5	3,963,096	231,208	5.51	6.47		
21X-3, 120-123	184.5	3,946,650	247,654	6.08			
21X-3, 120-123	184.5	3,872,529	321,775	7.81			
21X-CC, 11-13	186.4	3,913,823	280,481	6.82	6.36		
21X-CC, 11-13	186.4	3,949,064	245,240	5.90			
22X-1, 43-46	190.2	4,162,068	32,236	0.77	1.36		
22X-1, 43-46	190.2	4,154,762	39,542	0.97			
22X-1, 43-46	190.2	4,095,844	98,460	2.35			
22X-1, 112-115	190.9	3,878,361	315,943	7.53	7.44		
22X-1, 112-115	190.9	3,886,464	307,840	7.34			
22X-1, 112-115	190.9	3,881,831	312,473	7.45			
22X-2, 25-27	191.6	3,916,666	277,638	6.62	7.77		
22X-2, 25-27	191.6	3,820,055	374,249	8.92			
22X-3, 42-44	193.2	3,990,611	203,693	4.86	4.54		
22X-3, 42-44	193.2	4,017,882	176,422	4.21			
22X-3, 42-44	193.2	4,002,860	191,444	4.56			
22X-4, 101-104	195.3	3,847,910	346,394	8.46	4.77		
22X-4, 101-104	195.3	4,095,589	98,715	2.39			
22X-4, 101-104	195.3	4,053,249	141,055	3.46			
22X-5, 22-25	196.0	4,059,062	135,242	3.58	5.21		
22X-5, 22-25	196.0	3,907,049	287,255	6.85			
22X-CC, 10-12	198.1	3,899,840	294,464	7.02	7.58		
22X-CC, 10-12	198.1	3,880,417	313,887	7.48			
22X-CC, 10-12	198.1	3,848,292	346,012	8.25			
23X-3, 81-83	203.1	3,823,384	370,920	8.95	8.48		
23X-3, 81-83	203.1	3,862,128	332,176	8.00			
23X-1, 107-109	200.4	4,077,377	116,927	2.86	3.36		
23X-1, 107-109	200.4	4,035,925	158,379	3.87			
23X-1, 107-109	200.4	4,055,524	138,780	3.36			
23X-2, 40-43	201.2	4,023,135	171,169	4.11	4.68		
23X-2, 40-43	201.2	4,097,751	96,553	2.32			
23X-2, 40-43	201.2	3,886,333	307,971	7.61			
23X-4, 120-123	205.0	4,082,241	112,063	2.71	3.56		
23X-4, 120-123	205.0	3,996,805	197,499	4.71			
23X-4, 120-123	205.0	4,057,654	136,650	3.26			
23X-5, 59-63	205.9	4,174,639	19,665	0.47	1.35		
23X-5, 59-63	205.9	4,174,996	19,308	0.47			
23X-5, 59-63	205.9	4,064,536	129,768	3.10			

Table T1 (continued).

Core, section, interval (cm)	Depth (mbsf)	Not radiolarian-related porosity pixels	Radiolarian-related porosity pixels	Area radiolarian-related porosity (%)	Average area radiolarian-related porosity (%)	Average radiolarian-related porosity descriptive statistics
23X-6, 90-92	207.7	4,191,023	3,281	0.08	0.19	
23X-6, 90-92	207.7	4,178,720	15,584	0.38		
23X-6, 90-92	207.7	4,189,741	4,563	0.11		
23X-CC, 11-14	208.8	4,104,600	89,704	2.26	2.02	
23X-CC, 11-14	208.8	4,093,004	101,300	2.58		
23X-CC, 11-14	208.8	4,143,234	51,070	1.22		

Table T2. Radiolarian-related porosity data for décollement, Site 671.

Core, section, interval (cm)	Depth (mbsf)	Not radiolarian-related porosity pixels	Radiolarian-related porosity pixels	Area radiolarian-related porosity (%)	Average area radiolarian-related porosity (%)	Average radiolarian-related porosity descriptive statistics	
110-671C-							
1X-1, 115-118	496.9	4,124,866	69,438	1.656	1.36	Count	22
1X-1, 115-118	496.9	4,101,077	93,227	2.223		Maximum	4.64%
1X-1, 115-118	496.9	4,185,857	8,447	0.201		Mean	1.10%
1X-2, 138-140	498.6	4,062,426	131,878	3.144	4.64	Median	0.78%
1X-2, 138-140	498.6	3,982,615	211,689	5.047		Minimum	0.00%
1X-2, 138-140	498.6	3,954,076	240,228	5.727		Range	4.64%
1X-3, 88-91	499.6	4,104,187	90,117	2.149	1.34	Standard Deviation	1.15%
1X-3, 88-91	499.6	4,171,994	22,310	0.532			
1X-4, 114-116	501.3	4,073,713	120,591	2.875	2.16		
1X-4, 114-116	501.3	4,118,151	76,153	1.816			
1X-4, 114-116	501.3	4,119,282	75,022	1.789			
2X-CC, 18-21	512.1	4,137,084	57,220	1.364	1.18		
2X-CC, 18-21	512.1	4,152,400	41,904	0.999			
110-671B-							
54X-5, 49-52	498.2	4,184,272	10,032	0.239	0.82		
54X-5, 49-52	498.2	4,135,301	59,003	1.407			
54X-6, 102-104	500.2	4,166,986	27,318	0.651	1.04		
54X-6, 102-104	500.2	4,134,578	59,726	1.424			
55X-1, 5-68	501.9	4,130,496	63,808	1.521	1.52		
55X-2, 47-51	503.2	4,181,920	12,384	0.295	0.25		
55X-2, 47-51	503.2	4,190,508	3,796	0.091			
55X-2, 47-51	503.2	4,179,400	14,904	0.355			
55X-4, 130-133	507.0	4,190,181	4,123	0.098	0.28		
55X-4, 130-133	507.0	4,183,293	11,011	0.263			
55X-4, 130-133	507.0	4,174,622	19,682	0.469			
55X-5, 44-46	507.6	4,192,603	1,701	0.041	0.07		
55X-5, 44-46	507.6	4,191,773	2,531	0.060			
55X-5, 44-46	507.6	4,189,607	4,697	0.112			
55X-6, 136-138	510.1	4,189,537	4,767	0.114	0.13		
55X-6, 136-138	510.1	4,188,364	5,940	0.142			
55X-6, 136-138	510.1	4,189,083	5,221	0.124			
55X-7, 23-26	510.4	4,166,818	27,486	0.655	0.60		
55X-7, 23-26	510.4	4,176,533	17,771	0.424			
55X-7, 23-26	510.4	4,165,261	29,043	0.692			
55X-7, 23-26	510.4	4,168,357	25,947	0.619			
56X-1, 137-141	512.1	4,155,428	38,876	0.927	1.49		
56X-1, 137-141	512.1	4,143,241	51,063	1.217			
56X-1, 137-141	512.1	4,097,363	96,941	2.311			
56X-2, 60-63	512.8	4,193,027	1,277	0.030	0.08		
56X-2, 60-63	512.8	4,188,996	5,308	0.127			
56X-3, 120-123	514.9	4,181,285	13,019	0.310	0.47		
56X-3, 120-123	514.9	4,177,121	17,183	0.410			
56X-3, 120-123	514.9	4,165,158	29,146	0.695			
56X-4, 35-38	515.6	4,138,464	55,840	1.331	1.12		
56X-4, 35-38	515.6	4,121,140	73,164	1.744			
56X-4, 35-38	515.6	4,182,341	11,963	0.285			
56X-5, 102-105	517.7	4,135,251	59,053	1.408	0.75		
56X-5, 102-105	517.7	4,190,799	3,505	0.084			
56X-6, 60-63	518.8	4,149,891	44,413	1.059	0.63		
56X-6, 60-63	518.8	4,186,134	8,170	0.195			
56X-6, 60-63	518.8	4,167,216	27,088	0.646			
56X-7, 12-14	519.8	4,177,406	16,898	0.403	0.53		
56X-7, 12-14	519.8	4,149,601	44,703	1.066			
56X-7, 12-14	519.8	4,188,646	5,658	0.135			
58X-2, 116-118	532.4	4,194,304	0	0.000	0.00		
58X-4, 102-104	535.2	1,009,756	38,805	3.701	3.70		

Table T3. Interparticle porosity data for the clay matrix.

Depth (mbsf)	Solid area	Total image area	Void area	Interparticle porosity in clay matrix
Site 671				
517.7	33.52	46.60	13.08	0.281
517.7	33.52	46.60	13.08	0.281
517.7	32.37	46.60	14.23	0.305
496.9	33.31	46.60	13.29	0.285
498.2	28.55	46.60	18.05	0.387
512.1	26.64	46.60	19.96	0.428
498.2	29.03	46.60	17.57	0.377
535.2	29.03	46.60	17.57	0.377
535.2	35.27	46.60	11.33	0.243
500.2	35.13	46.60	11.47	0.246
Average:	31.64	46.60	14.96	0.321
Site 672				
169	18.79	46.60	27.81	0.597
172.8	16.00	46.60	30.60	0.657
190.9	16.37	46.60	30.23	0.649
191.6	13.57	46.60	33.03	0.709
193.2	15.14	46.60	31.46	0.675
205	19.30	46.60	27.30	0.586
Average:	16.53	46.60	30.07	0.645